Massive sediment pulses triggered by a multi-stage alpine cliff fall (Hochvogel, DE/AT)

Natalie Barbosa[1,2], Johannes Leinauer[2], Juilson Jubanski[3], Michael Dietze[4,5], Ulrich Münzer[6], Florian Siegert[1,3], Michael Krautblatter[2].

5 [1]Department of Earth and Environmental Sciences, Faculty of Earth Sciences, GeoBio Center, Ludwig-Maximilians-University, Munich, 80333, Germany.
[2]Chair of Landslide Research, Technical University of Munich, Munich, 80333, Germany
[3]3D RealityMaps GmbH, Munich, 81673, Germany
[4]Faculty of Geosciences and Geography, Georg-August-Universität Göttingen, Göttingen, 31073, Germany
10 [5]GFZ German Research Centre for Geosciences, Potsdam, 14473, Germany
[6]Department of Earth and Environmental Sciences, Section Geology, Ludwig-Maximilians-University, Munich, 80333, Germany.

Correspondence to: Natalie Barbosa (barbosa@biologie.uni-muenchen.de)

15 **Abstract**

Massive sediment pulses in catchments are a key alpine multi-risk component. Substantial sediment redistribution in alpine catchments frequently causes flooding, river erosion, and landsliding, and affects infrastructure such as dam reservoirs as well as aquatic ecosystems and water quality. While systematic rock slope failure inventories have been collected in several countries, the subsequent cascading sediment redistribution is virtually unaccessed.

20 This contribution reports for the first time the massive sediment redistribution triggered by the multi-stage failure of more than 150,000 m³ from the Hochvogel dolomite peak during the summer of 2016. We applied change detection techniques on seven 3D-coregistered high-resolution true-orthophotos and digital surface models (DSM) obtained through digital aerial photogrammetry later optimized for precise volume calculation in steep terrain. The analysis of seismic information from surrounding stations revealed the temporal evolution of the cliff fall.

25 We identified the proportional contribution of >600 rockfall events (>1 m³) from 4 rock slope catchments with different aspects and their volume estimates. In a sediment cascade approach, we evaluated erosion, transport, and deposition from the rockface to the upper channelized erosive debris flow channel, then to the widened dispersive debris flow channel, and finally to the outlet into the braided sediment-supercharged Jochbach river. We observe the decadal flux of more than 400,000 m³ of sediment with massive sediment pulses that (i) respond with reaction 30 times of 0-4 years and relaxation times beyond 10 years, (ii) with faster response times of 0-2 years in the upper catchment and more than 2 years response times in the lower catchments, (iii) the inversion of sedimentary (10²-10³ mm/a) to massive erosive regimes (10² mm/a) within single years and the (iv) dependency of redistribution to rainfall frequency and intensity. This study provides generic information on spatial and temporal patterns of massive sediment pulses in highly-charged alpine catchments.

35

Keywords

large format aerial photogrammetry, rockfall, massive sediment redistribution, increased debris flow activity, alpine catchment, Hochvogel.

40

Introduction

Mechanisms and scales of sediment propagation throughout space and time in sediment cascades are paramount
to the development of prevention and mitigation measures. Several studies have focused on sediment cascades on
fluvial landscapes (e.g., (Burt and Allison, 2010; Joyce et al., 2018)) however, few quantitative studies have been
undertaken in active mountain environments controlled by landsliding (e.g., (Wichmann et al., 2009; Heckmann
et al., 2016; Clapuyt et al., 2019). Landslides provide and condition the input of sediment volumes. Despite their
relevance in the sediment cascades, landslide deposit residence times, cascade sediment pulses, and redistribution
controlling factors are rarely quantified due to the sudden, unpredictable, and spatially distributed occurrence.

Sediment delivery from rockfalls to the drainage network has significant implications for catchment scale
sediment fluxes and landform evolution (Benda and Dunne, 1997; Tucker, 2004). Despite this, there is a lack of
systematic studies focused on the short-term temporal and spatial development of mechanisms that link and
maintain sediment continuity within hillslopes. Attempts to better understand short-term erosion rates and
sediment yield at a basin scale include spatial pattern analysis (Schrott et al., 2003), sediment budgets (Joyce et
al., 2018), numerical modeling (Wichmann et al., 2009; Heckmann and Schwanghart, 2013), and application of
the connectivity framework (Wichmann et al., 2009; Fryirs, 2013). These approaches incorporate both spatial and
temporal variability in the operation of the sediment cascades at a diversity of scales, however, lack key
observations on rare and high-magnitude events. On the other hand, debris flows serve as a link to hillslope-
channel coupling by connecting large parts of rock walls to the channel network (Heckmann and Schwanghart,
2013). Debris flows rapidly mobilize $< 10^2$ to $>10^9$ m^3 of sediment (Jakob, 2005) along great distances reaching
infrastructure and populated areas. While debris flows are typically considered transport-limited processes
(Gregory and Lewin, 2014), numerical simulations suggest that continuous delivery of sediment from upslope
areas to the location where debris flows are initiated maintains the supply of material available for transport, thus,
impacting the persistence and magnitude of sediment pulses in the system(Heckmann and Schwanghart, 2013).
Several studies have collected data from massive rock slope failures (e.g., (Dussauge-Peisser et al., 2002;
Heckmann et al., 2012; Fischer et al., 2012; Krautblatter et al., 2012; Guerin et al., 2020) which are a major
landscape evolution process and significantly contribute to sediment yields by sporadic production of a
considerable ($<10^3$ m^3 km^2 yr^{-1}) amount of debris (McSaveney, 2002; Korup et al., 2010; Krautblatter et al., 2012).
However, few studies have quantitatively assessed the subsequent cascading sediment redistribution and reaction
and relaxation times in highly active alpine catchments. Recent high-magnitude rockfalls in the European Alps
raised attention to the potential of catastrophic cascading sediment transport. The 2011 and 2017 rockslides in the
upper Val Bondasca, Swiss Alps, were preceded by an unusually high debris flow activity that reached the town
of Bondo (Baer et al., 2017; Mergili et al., 2020). A total of 99 buildings were damaged by the multiple debris
flows that occurred on August 2017 with an assumed economical loss of around 41 million francs (NNZ, 2017).
In the coming decades with enhanced rainstorm activity, massive sediment redistribution in alpine catchments
will be a key hazard and challenge in alpine communities, thus, constraining rates and sediment cascades response
times to suddenly increased sediment input by landsliding is paramount for prediction and early warning.

This paper reports the massive sediment redistribution triggered by the multi-stage failure from the Hochvogel
dolomite peak during the summer of 2016. We evaluate the spatio-temporal morphodynamics at a catchment scale

before and after the cliff fall by means of multi-temporal high-resolution aerial photogrammetry between 2010 and 2020. The (multi-) annual photogrammetric surveys provide information on detachment areas and failed volumes, but the time resolution is limited to the recurrence interval between two consecutive surveys. To overcome this limitation, we use high-resolution seismic records capturing relevant rockfall events (e.g., (Hibert et al., 2011; Lacroix and Helmstetter, 2011; Manconi et al., 2016; Fuchs et al., 2018; Dietze et al., 2017a)). The combination of seismic information with high-resolution wide-extent photogrammetric reconstructions resulted in (i) identification of the spatial and temporal contribution of rockfall material from the four rock slope catchments that constitute the Hochvogel summit, (ii) quantification of (multi-) annual series of sediment budgets erosion rates before and after the cliff fall evidencing the dramatic inversion of deposition and erosion processes, (iii) time series of sediment cascading and (iv) estimation of the system reaction time and redistribution controls with respect to rainstorm intensity and frequencies. To our knowledge, this paper is the first to show the cascading sediment response of an alpine catchment to a massive rock slope failure. This enables a better understanding of catchment morphodynamic responses to high magnitude rock fall, propagation, and persistence of sediment waves through alpine catchment system and future hazard scenarios where increased sediment availability and seasonal extreme heavy rainfall are expected.

2 Study area

The Hochvogel peak (47°21'N, 10°26'E, 2592 m a.s.l), is a prominent summit in the Northern Calcareous Alps and a popular destination for hikers. The Hochvogel massif consists of Hauptdolomit, a brittle, variably bituminous carbonate rock with pronounced bedding (dm-m) and incidental marly interlayers. The rock mass is tectonically stressed and highly weathered. A meter-size fracture at the summit poses a catastrophic rock failure scenario (Leinauer et al., 2020, 2021) directly impacting the Weittal valley (Figure 1).

Four slopes constitute the pyramidal-shaped summit with orientations towards northeast, west, southeast, and southwest and mean inclinations between 43° to 47°. The southwestern slope is distinguished by its current almost vertical wall and upper negative slope reaching the peak of the summit. Slope processes occurring at the southwestern slope are transferred to the Weittal catchment which extends over 1.9 km² with an elevation difference of more than 1,300 m. The area directly affected by slope instabilities occurring at the southwestern slope covers 378,642 m² between 2010 to 2021 and is divided into four morpho-dynamic components (Figure 1a) **rock face:** with strong slope changes, serve as the source of sediment production (primary and secondary rockfalls), **upper channelized erosive debris flow channel:** characterized by a mean slope of 42°, promotes temporal accumulation of sediment in an incipient slope talus. A confined asymmetric valley follows the slope talus limited to the east by vertical walls of almost 60 m in height. At the same time, to the west, sporadic minor pulses of sediment are produced by erosion of the base of an older slope deposit gently oriented southwest. **widened dispersive debris flow channel:** geographically limited by the intersection of the Weittal and Wildenbach streams, starts by a rock wall confined valley which transforms into a highly active unconfined slope under continuous incision of older deposits and the **outlet** into the Jochbach river which imposes a high sediment transfer regime evidenced in the braided development of the river along an alluvial plain with a mean inclination of 14° and the presence of terraces with a height between 1 to 3 m from the current main channel.

Rockfalls on the southeastern and southwest slopes of the Hochvogel summit were documented in 1934, 1935, 2005, and 2007 (DAV, 2017). Between Saturday 9 and Monday 11 of July 2016 (Heißel and Figl, 2017), noises and a dust cloud alerted the local authorities due to a new rockfall event that affected the Weittal valley (Figure 125 1. b and c.).
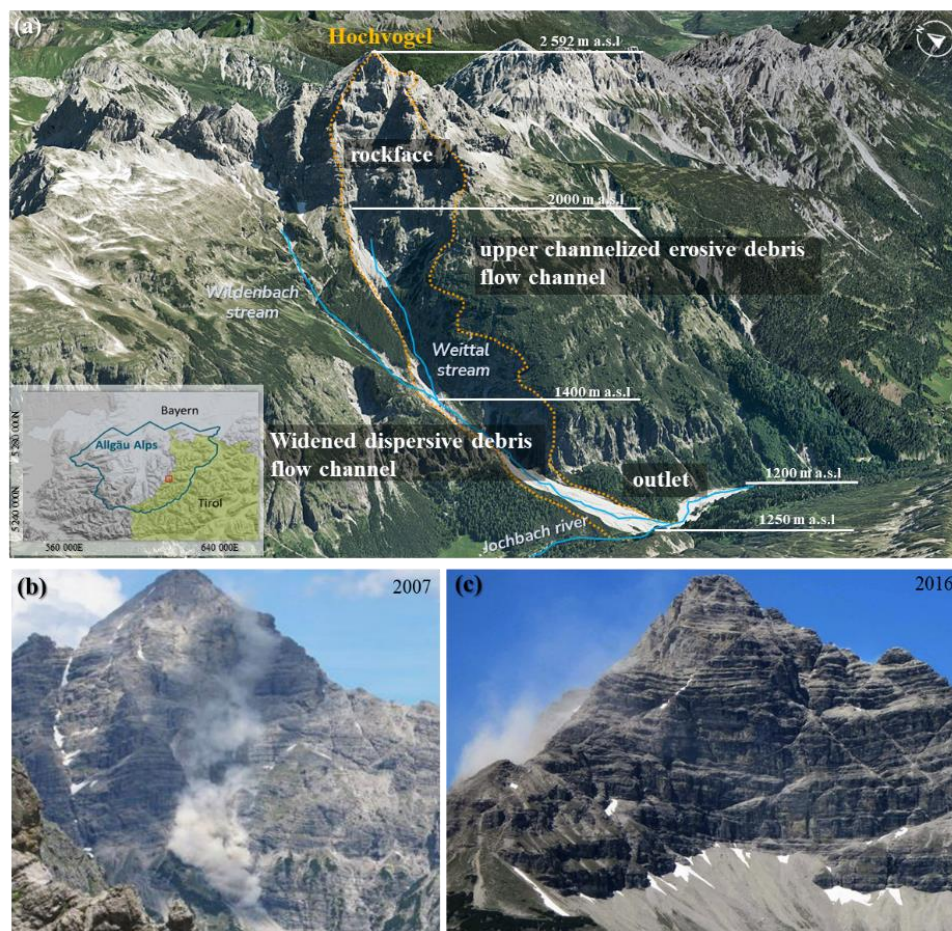
Figure 1. a) Location of the Hochvogel summit in the Allgäu Alps between Bavaria (Germany) and Tirol (Austria) and 3D-reconstruction of the southwest slope indicating the approximate elevation of the boundaries of the morphodynamic components: rockface, upper channelized erosive debris flow channel, widened dispersive debris flow channel, and 130 outlet. The orange line delimits the 378,642 m² impacted by the cliff fall studied in this contribution. b) Dust cloud over the southwest slope produced by the 2007 rockfall event (DAV, 2017) b) southeastern slope with remnant dust cloud from the 2016 rockfall event at the southwest slope (DAV, 2016).

3. Methods

3.1 Multi-temporal quantification of surface change

135   We used large format aerial imagery surveyed by the Austrian and German Cartographic Survey offices (BEV & LDBV) and by 3D RealityMaps GmbH to investigate the spatial and temporal sediment production, transport, and accumulation patterns of the southwest slope of the Hochvogel in 6 intervals over ten years. All seven surveys (09.2010, 08.2012, 09.2014, 06.2015, 08.2017, 09.2018, and 08.2020) have a nominal 20 cm spatial resolution (supplementary Table 1.) for the production of the digital surface models (DSM) and true orthophotos from the

140   photogrammetric point clouds. The produced DSMs were aligned to the reference dataset acquired on 21.09.2018 by means of a 3D-coregistration for the further application of change detection and volume calculation.

3.1.1 2.5D topographic time series

    The photogrammetric workflow to generate DSM and true orthophoto from nadir view aircraft photographs consist of the initial standardization of the aerotriangulation provided by the survey agencies into the same spatial

145   reference system using the software Inpho and Match-AT by Trimble, and followed by the generation of oriented point clouds, DSM, and orthophotos using the semi-global matching algorithm first developed by (Hirschmuller, 2008) and implemented in the software SURE from nFrames (ESRI) (Haala and Rothermel, 2012; Rothermel et al., 2012). We optimized the orthophotos and DSMs for a more precise volumetric calculation in steep terrain by the application of a 7-parameter 3D similarity transformation described by (Eq. (1)). To minimize the 3D distance

150   between a reference surface (21.09.2018) and the interest datasets, we manually selected 30 multi-temporal well-distributed 3D corresponding points (x, y, z) located in stable, non-changeable areas using the true orthophotos and the corresponding DSMs, and solved Eq. (1) using the least-squares adjustment solution in python.

$$\begin{bmatrix} x_{obs} \\ y_{obs} \\ z_{obs} \end{bmatrix} = \lambda \begin{bmatrix} cos(\varphi)cos(\kappa) & sin(\omega)sin(\varphi)cos(\kappa) - cos(\omega)sin(\kappa) & cos(\omega)sin(\varphi)cos(\kappa) + sin(\omega)sin(\kappa) \\ cos(\varphi)sin(\kappa) & s \in (\omega)sin(\varphi)sin(\kappa) + cos(\omega)cos(\kappa) & cos(\omega)sin(\varphi)sin(\kappa) + sin(\omega)cos(\kappa) \\ -sin(\varphi) & s \in (\omega)cons(\varphi) & cos(\omega)cos(\varphi) \end{bmatrix} \begin{bmatrix} x_{ref} - x_0 \\ y_{ref} - y_0 \\ z_{ref} - z_0 \end{bmatrix} \quad (1)$$

    where $[x_{obs}, y_{obs}, z_{obs}]^T$ and $[x_{ref}, y_{ref}, z_{ref}]^T$ are the vectors of coordinates of the corresponding points at the

155   search surface $s(x, y, z)$ and reference surface $r(x, y, z)$ with size $(1, 3 * n_{correspoding\ points})$ respectively ; λ is the uniform scale factor; $[x_0, y_0, z_0]^T$ is the vector of approximate values of the parameters; and ω, φ, κ represent the rotation Euler Angles used to calculate the orthogonal rotation matrix $m_{ij} = M(\omega, \varphi, \kappa)$. Parameters λ and $[x_0, y_0, z_0]^T$ are initially approximated to 0 and $M(\omega, \varphi, \kappa)$ to $\frac{\pi}{180}$. The evaluation of the estimated parameters $M(\omega, \varphi, \kappa)$, λ and $[x_0, y_0, z_0]^T$ after the convergence of the model (5 iterations) results in the elimination of

160   outliers and the warranty of randomness in the residual values defined as the difference between the $r(x, y, z)$ and $s_{trans}(x, y, z)$, being s_{trans} the new coordinates of the corresponding points at the search surface after the application of the transformation parameters (Figure 2).

Earth **Surface**
Dynamics
Discussions
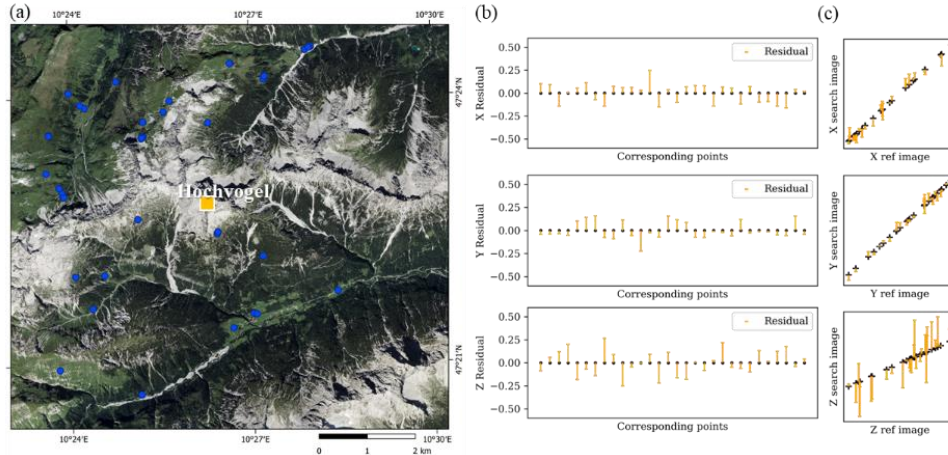
Figure 2. a) True orthophoto of the reference surface acquired on 21.09.2018. Blue dots indicated the corresponding

165   **points with the search surface acquired on 07.08.2017. Similar spatial distribution is followed for the remaining datasets according to the extent of the acquisition. b) Residuals calculated as the difference between the $r(x, y, z)$ and $s_{trans}(x, y, z)$, being s_{trans} the new coordinates of the corresponding points at the search surface after the application of the transformation parameters for each spatial axis x, y, and z. c) Spatial distribution of the corresponding points at each spatial axis x, y, and z.**

170   Repetitive topographic surveys, in our case DSMs, allow the identification and quantification of geomorphic changes such as erosion and deposition (James et al., 2012; Wheaton et al., 2010). We estimated the area and volume of change based on 2.5 data., i.e., rasterized topography following Eq. (2):

$$DoD = Z_{new} - Z_{old} \quad (1)$$

175   where DoD is the difference of elevation between consecutive DSMs (Z_{new} and Z_{old}). Despite the limited depiction of vertical walls and possible artifacts for overhanging walls, gridded datasets, i.e., DEM, support the fast and straightforward calculation of 2.5 D volumes by Eq. (3):

$$V = a \sum_{i=1}^{n} DoD_i \quad (3)$$

$$\text{where} \quad a = n * a_{pixel} \quad (4)$$

180   and n is the number of pixels conceding with a change, a_{pixel} corresponds to 0.4 m^2, and DoD_i is the elevation difference between time periods.

We used the non-interpolated DSMs to minimize the change to noise ratio (Wheaton et al., 2010; Anderson, 2019). Elevation uncertainty of photogrammetric surveys is roughly assessed as three times the spatial resolution,

185   however, lighting conditions, surface roughness, and camera configuration among others, imprint an inhomogeneous spatially distributed uncertainty which estimation remains challenging. We evaluated the elevation uncertainty after the 3D-coregistration using 30 independent well-distributed points on stable areas with complex topography (supplementary Table 2). The elevation uncertainty, measured as the RMSE of the elevation difference in stable areas with complex topography, ranges between 30 to 40 cm (supplementary Table 3). We

190   segmented the study area into four regions based on morphometric characteristics, to acknowledge the role of topography on elevation uncertainty. Hereby slope angle and slope aspect, influence the minimum detectable

change through time but also imprint morphodynamic characteristics (Sect. 2.). Conservative critical thresholds above the measured coregistration error and elevation uncertainty for each region were determined by best practice between 0.2 to 1 m (supplementary Table 4 and 5).

195

We filter the different sources of topographic changes by semi-automatic filtering, and final manual inspection using 3D visualization. The filtering processes are based on the segmentation of the DoD using a 3x3 circular kernel on a binary mask of change (1)-no change (0) defined by the critical thresholds. The size of the kernel was selected to segment an approximate connected change of a minimum of 1 m². We used descriptive statistical

200 information from each polygon: minimum and maximum elevation change, area of change, volume of change, and mean slope before the change, to filter the polygons using the criteria described in Table 1. The slopes at the Hochvogel are mostly highly-fractured and horizontally layer, thus, rock falls preferentially follow a pseudo-cubic form. Hence, the filtering approach focuses on the identification of changes that are over-elongated in the z component in relation to their horizontal area (area/maximum elevation change <1). These types of changes are

205 identified as "false" rockfalls. A 3D visualization supports the final visual inspection.

Table 1. Attributes, argumentation, and threshold value used to filter the change polygons from noise. Threshold values are selected by visual inspection of the filtering results. (A) rockface, (B) Upper channelized erosive debris flow channel, (C) Widened dispersive debris flow channel, and (D) outlet.

Attribute	Usage	Threshold value
Area/Maximum elevation change	Detection and elimination of vertical changes that correspond to poor edge depiction.	< 1
Mean slope before the change	Differentiation of erosion and deposition area based on physical parameters.	Erosion at (A) and (B) is limited to slopes with > 30° Erosion at (C) occurred on slopes > 5° Deposition at (A), (B) and (C) is limited by the repose angle of calcareous materials approximated to < 50°
Number of pixels of change	Detection of small changes which are prone to higher uncertainty and visually inconclusive.	> 15 connected pixels

210 The 3D-coregistration process suggest a neglectable horizontal error at the pixel level, thus, the total volume uncertainty (δV) from Eq (3) is the sum of the uncertainty of each cell of volume (δv) calculated such Eq (5) :

$$v = a_{pixel}DoD_{pixel} \text{ (5)}$$

To propagate the errors of each cell of volume, the partial derivative of Eq (5) with respect to the elevation change, which is the variable that has uncertainty, is calculated:

215

$$\delta v = |v'(DoD)|\delta_{DoD} \text{ (6)}$$

$$\text{where } \delta_{DoD} = RMSE_{Z_{time\ period}}$$

Finally, the volume uncertainty over area A is given by Eq. (7):

$$\delta V = A\delta v \text{ (7)}$$

3.1.2 Frequency-magnitude curves

220 A frequency-magnitude curve relates the magnitude of a variable to the frequency of occurrence (Riggs, 1968). The curve is an estimate of the incremental yearly cumulative frequencies from the largest magnitude event to the smallest (Hungr et al., 2008). We included both primary and secondary rockfalls in our analysis. We acknowledge the occurrence of coalescence events, given the (multi-) yearly temporal resolution of the datasets. The frequency analysis aims to compare the activity and relative size distribution (Dussauge-Peisser et al., 2002; Benjamin et al.,

225 2020; Hantz et al., 2021) of the different rock faces slopes that constitute the Hochvogel summit.

3.1.3 Cascading geomorphic sediment budgets

A sediment budget describes the input, transport, storage, and export of sediment in a geomorphic system. This

230 concept provides an effective basis for representing the key components of the sediment delivery system within a catchment and for assembling the necessary data to elucidate, understand and predict catchment sediment delivery (Walling and Collins, 2008) and estimate related natural hazards. The geomorphic sediment budget (Wheaton et al., 2010) is calculated as the sum of the masked DoD values of erosion (negative change) and deposition (positive change).

235

We calculate the proportion of net erosion and net deposition per year ($m^3 y^{-1}$) based on the number of days between acquisitions, comparable to previous studies. Conversion to mass (t) is based on reported densities of limestone 2.6 t m^3 and limestone deposits 2 t m^3 according to (Krautblatter et al., 2012). Spatially averaged short-term wall retreat rates were calculated by dividing the total rockfall volume per year ($m^3 y^{-1}$) by the area over

240 which the volumes were calculated., i.e., northern slope (253,643 m^2), western slope (115,098 m^2), southwestern slope (254,686 m^2), southeaster slope (165,037 m^2), rockface (234,329 m^3), upper channelized erosive debris flow channel (53,072 m^3), widened dispersive debris flow channel (91,241 m^3) and outlet (34,004 m^3).

3.2. Volume estimation of the 2016 multi-event

3.2.1. 3D cumulative volume

245 The 2016 rockfall dramatically changed the morphology of the southwestern slope of the Hochvogel. A visual comparison of images taken by Land Tirol during a helicopter flight inspection to the summit on 03.07.2015 and the UAV images acquired by the landslide group (Andreas Dietrich) at the Technical University of Munich (TUM) using a UAV DGI Phantom 4 during a monitoring survey as part of the AlpSenseBench project on 28.09.2017, revealed the pre-event topography of the southwestern slope (Figure 3). Recent developments in dense matching

250 algorithms in combination with structure from motion (SfM) retrieve dense point clouds (Eltner and Sofia, 2020). For a more precise reconstruction of 3D geometry of the cliff fall, particularly on the vertical slopes, we calculated the volume of change using the most complete photogrammetric point clouds from an acquisition before the event, 23.09.2014, and after the event, 07.08.2017. We manually delimited the extent of the 2016 rockfall event based on the cloud-to-cloud distance algorithm in CloudCompare v2.0. The volume calculation was performed over a

255 grid of 0.2 cm and an average height cell in CloudCompare v2.0. For visualization purposes, we reconstructed the detached surface by creating a mesh using the Poisson Surface Reconstruction plugin (Kazhdan et al., 2020) and

the two-point clouds. The approximate orientation of fractures was extracted from the photogrammetric point cloud 23.09.2014 using the CloudCompare plugging Compass (Thiele et al., 2017).

3.2.2. Multi-stage detachment analysis

260 For the time interval in which the 2016 failure occurred (July 9 to 11), we downloaded all available seismic data from seven surrounding broadband stations (distance to Hochvogel: 12-55 km) (supplementary table 7). By analyzing the local seismic amplitude and the corresponding spectrograms at each station, we identified all seismic events with the strongest impact at the closest station in Oberstdorf. Rock falls produce a seismic impact over all frequencies between 5 and 50 Hz Dietze et al., 2017; Le Roy et al., 2019); in our case, we expect a clear decrease

265 in seismic intensity with increasing distance of the stations from the Hochvogel and significant arrival time differences of up to 20 s (supplementary Fig. 3). On the contrary, earthquakes often show distinct arrivals of P and S waves, a lower frequency content, and smaller arrival time differences. Local anthropogenic noise is characterized by higher frequency contents and missing coincidence of the signal between different stations. Following these criteria, we identified all potential seismic signals originating from the rock fall series at the

270 Hochvogel.

Despite significant variability in the scaling of E_p to E_S (cf. (Hibert et al., 2011), Le Roy et al., 2019 determined a relation between generated seismic energy Es and the potential energy of a rock fall Ep such:

$$E_s = 10^{-8} \times E_p^{1.55} \quad (11)$$

275 The initially failed volume can then be derived from the potential energy if we determine the fall height of the block that generated the seismic signal. We estimated the fall height of the rock fall event from the photogrammetric point cloud differences and 3D models. A simple toppling of the center of gravity towards the slope corresponds to a fall height of 50-60 m while a sliding of the failed block suggests a probable fall height of 75 to 100 m. The calculation of the seismic energy and the determination of all needed parameters mainly follows

280 the methodology in Le Roy et al., 2019 (supplementary Sec. 2). We estimated the error of the calculations based on Monte Carlo simulations with 1000 iterations and the variability of the different stations.

4. Results

4.1 Multi-stage occurrence of the 2016 cliff fall event

285 The cliff fall that occurred during the summer of 2016 resulted in the detachment of 1.31 ($\pm$0.01) *10^5 m^3 of dolomite following a multi-stage development. The extent of the cliff detachment is indicated by the clearer color tone on the rock surface (Fig 3b.), and the detachment area was measured to be 4,777 m^2 using a combination of photogrammetric derived point clouds before and after the cliff fall. Prior to the cliff fall, the area was characterized by a vertical rock tower surrounded by pervasive fractures with orientation NW and pseudo-vertical

290 dip angles that may have contributed to the multi-stage detachment by widening preexisting rock discontinuities (Figure 3a). The rock tower had a height exceeding 60 meters and was a prominent feature in the landscape. Currently, partially disconnected blocks are limited by penetrative fractures and represent areas of potential detachments. The cliff fall resulted in a significant change in the morphology of the southwest slope increasing the mean slope by 1° from 45.6° to 46.6°.

Earth **Surface**
Dynamics
Discussions

295
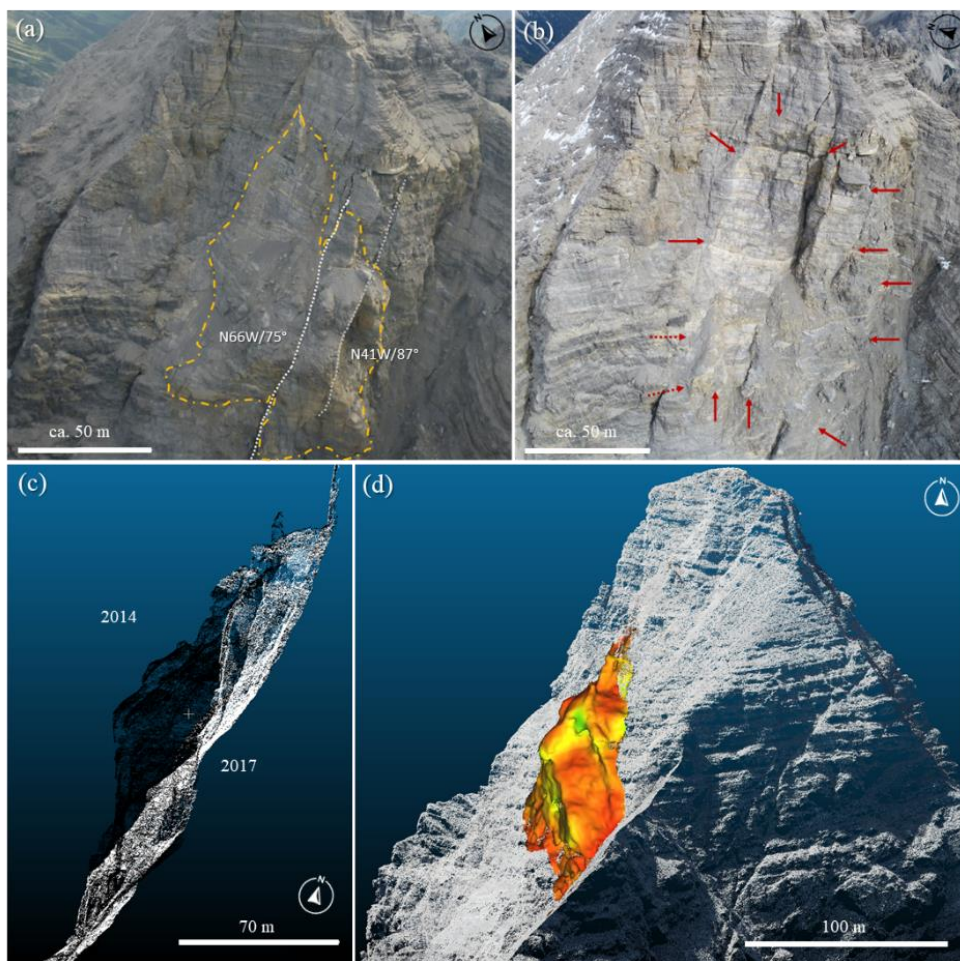
Figure 3. Picture taken by Land Tyrol before the cliff fall (03.07.2015). The yellow line indicates the cliff fall detachment area in the summer of 2016. The fracture orientations (in white) intend to exemplify approximate structure orientation and must be taken with caution due to the low point density in the exposed fracture surfaces. b) Picture taken by TUM Landslides group (Andreas Dietrich) after the cliff fall (28.09.2017). The red arrows indicates the cliff fall detachment
300 **area in the summer of 2016 c) Photogrammetric point clouds from the surveys on 23.09.2014 in black and 07.08.2017 in white. d) Mesh reconstruction of the cliff fall.**

The seismic signal analysis indicates a progressive failure of the total mass in at least three to six portions within 3 days (Table 2). The biggest parts of the rock mass failed on the last day (2016.07.11) at 20:48, 21:05, and 21:07 local time. The volume estimation from the seismic energy at the closest station in Oberstdorf (OBER) results in
305 a median volume of 1.02 ($\pm$0.09) $*10^5$ m^3 for a fall height of 60 m. The estimated volume excludes smaller rockfalls, since the limited energy released by these events may not been recorded by the seismic stations. As a result, the seismically estimated volume may underestimate the total amount of material detached.

Table 2. Temporal multiphase cliff fall detachment between July 9th and 11th 2016 at the Oberstdorf station (OBER). Detected event phases and partial volumes (given as median ± sd).

Event	First arrival time at OBER in UTC	Status	Mean volume from station OBER with fall height = 60 m [m³]
1	2016-07-09 08:37:45	probably rock fall signal	$8.92 \, (\pm 1.52) \times 10^3$
2	2016-07-09 17:39:27	probably rock fall signal	$1.96 \, (\pm 0.32) \times 10^3$
3	2016-07-11 17:39:36	probably rock fall signal	$2.83 \, (\pm 0.54) \times 10^3$
4	2016-07-11 18:48:13	clearly rock fall signal	$1.74 \, (\pm 0.30) \times 10^4$
5	2016-07-11 19:05:19	clearly rock fall signal	$1.83 \, (\pm 0.32) \times 10^4$
6	2016-07-11 19:07:16	clearly rock fall signal	$5.25 \, (\pm 0.88) \times 10^4$
		SUM	$1.02 \, (\pm 0.09) \times 10^5$
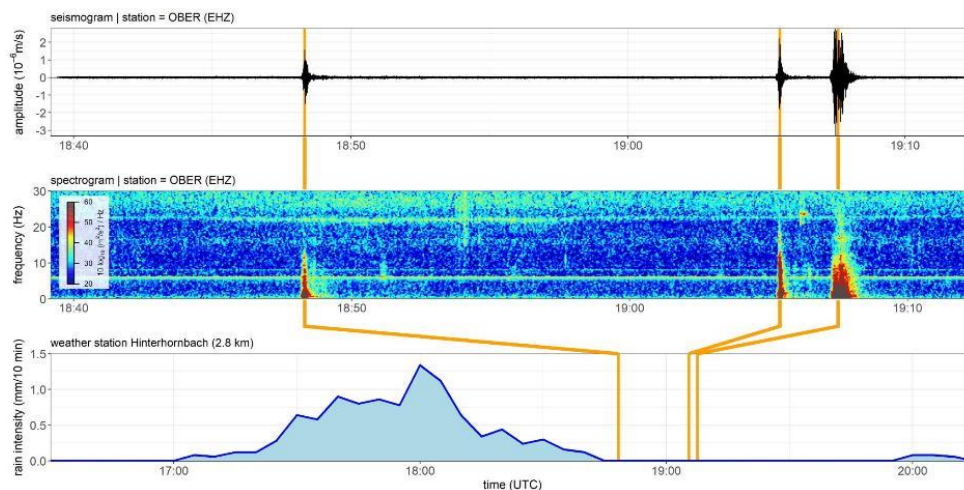
Figure 4. Unmistakable rock detachments on 11th July at the Oberstdorf seismic station (OBER) a) Amplitude of the seismic signal b) spectrogram covering all frequencies up to 30 Hz. c) rainfall intensity at Hinterhornbach (mm/10 min) before and after the rock detachments.

4.2 Summit slope erosion

Over the last decade, the Hochvogel summit has produced $1.713 \, (\pm 0.04) \times 10^5$ m³ of sediment, corresponding to an annual production rate of 43,990 ($\pm$ 1 069) t y^{-1} when assuming a rock density of 2 600 kg m^{-3} (Krautblatter et al., 2012). Notably, 97% of this sediment can be attributed to the 2016 cliff fall at the Southwestern slope. A total of 667 erosional events, including primary and secondary rockfalls, were detected at the Hochvogel summit, with a median volume ranging between 4.6 to 9.3 m³. The minimum detectable rockfall volume ranged between 1.4 to 2.1 m³, depending on the slope orientation. The sediment production on the four slopes of the summit showed a significant disproportion. The western and southeastern slopes had the lowest rockfall frequency, while the northern slope experienced the highest rockfall activity per year (Figure 5). However, when considering the

325 contribution of rockfall magnitudes, debris falls dominate the northern and western slopes, while the southeaster slope has a larger proportion of boulder fall, accounting for 55% of the total contribution (Table 3).
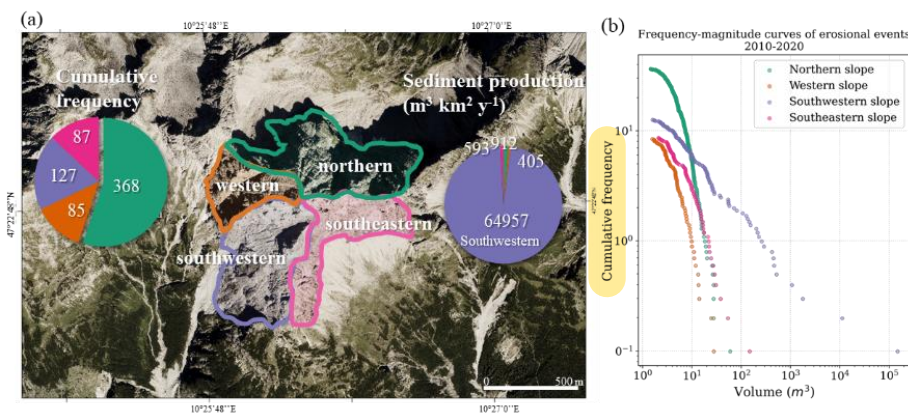
Figure 5. Erosional events between 2010 and 2020. i.e., primary and secondary rockfalls grouped by slope
330 orientation. a) slope orientation. b) Magnitude-Frequency curves.

Table 3. Contribution of rockfall magnitudes. Volumetric classification based on *(Whalley, 1974, 1984; Erismann and Abele, 2001; Krautblatter et al., 2012)*. * Error equal to total volume percentage error. Rockwall retreat refers to the horizontal retreat of the vertical rockcliff

	northern slope 253 643 m²		western slope 115 098 m²		southwestern slope 254 686 m²		southeastern slope 165 037 m²		Total (m³)
	Total (m³)	(%)	Total (m³)	(%)	Total (m³)	(%)	Total (m³)	(%)	
Debris fall Volume < 10 m³	$1.53\ (\pm 0.03)\ *10^3$	65	$3.34\ (\pm 0.08)\ *10^2$	71	$3.37\ (\pm 0.08)\ *10^2$	0	$3.01\ (\pm 0.07)\ *10^2$	30	$2.50\ (\pm 0.06)\ *10^3$
Boulder fall $10 < \text{Volume} < 10^2$ m³	$8.11\ (\pm 0.20)\ *10^2$	35	$1.38\ (\pm 0.03)\ *10^2$	29	$1.17\ (\pm 0.02)\ *10^3$	1	$5.41\ (\pm 0.13)\ *10^2$	55	$2.54\ (\pm 0.06)\ *10^3$
Block fall $10^2 < \text{Volume} < 10^4$ m³	0	0	0	0	$6.57\ (\pm 0.16)\ *10^3$	4	$1.48\ (\pm 0.04)\ *10^2$	15	$6.72\ (\pm 0.14)\ *10^3$
Cliff fall $10^4 < \text{Volume} < 10^6$ m³	0	0	0	0	$1.59\ (\pm 0.03)\ *10^5$	95	0	0	$1.59\ (\pm 0.03)\ *10^5$
Total volume (m³)	$2.34\ (\pm 0.03)\ *10^3$		$4.72\ (\pm 0.07)\ *10^2$		$1.67\ (\pm 0.04)\ *10^5$		$9.90\ (\pm 0.24)\ *10^2$		$1.71\ (\pm 0.04)\ *10^5$
Volume per year (m³ y⁻¹)*	$2.31\ (\pm 0.06)\ *10^2$		$4.6\ (\pm 0.10)\ *10^1$		$1.65\ (\pm 0.04)\ *10^4$		$9.7\ (\pm 0.20)\ *10^1$		$1.69\ (\pm 0.04)\ *10^4$
Rockwall retreat (mm y⁻¹)	**0.9**		**0.4**		**64**		**0.5**		

4.3. Geomorphic sediment budget

335

The short-term denudation rates in the catchment prior to the cliff fall were 45 to 52 mm y⁻¹, resulting in a negative catchment sediment budget ranging $-1.72\ (\pm 0.01)\ *10^4$ m³ y⁻¹ and $-1.97\ (\pm 0.01)\ *10^4$ m³ y⁻¹. Following the cliff fall, the catchment's denudation rates increased abruptly by ten times, reaching 257 mm y⁻¹. Despite the erosion of $9.74\ (\pm 0.01)\ *10^4$ m³ y⁻¹, the sediment delivery to the outlet was significantly reduced, resulting in a positive

340 catchment sediment budget of 1.306 (±0.06) $*10^4$ m^3 y^{-1} (Figure 6).However, two years after the event, within catchment sediment waves dominated the sediment flow to the outlet leading to a negative sediment budget of - 1.033 (±0.08) $*10^4$ m^3 y^{-1}. Subsequently, a slightly positive sediment budget of 6.12 (±2) $*10^2$ m^3 y^{-1} evidenced the ongoing sediment redistribution within the catchment four years after the cliff fall, even though, the catchment denudation rates returned to pre-event levels of 44 mm y^{-1}. Catchment scale erosion and deposition volumes at

345 each time interval are listed in Table 4.
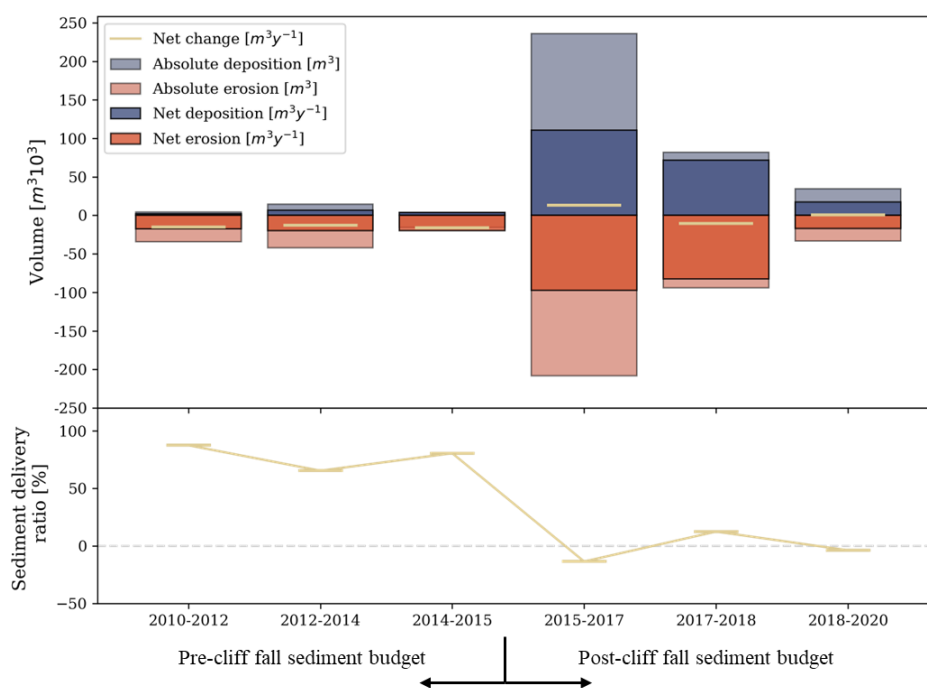
Figure 6. Time series of geomorphic sediment budgets at the catchment. The bar plot depicts yearly volumes of erosion in red and deposition in blue. The yellow line indicates the net change calculated as the difference between erosion and deposition at each time interval. The estimated uncertainty of the absolute volume is less than 1%, thus,
350 **imperceptible due to the scale of the graph. The sediment delivery ratio is expressed as the proportion of sediment leaving the basin and the total net erosion.**

Table 4. Catchment scale erosion, deposition and net volumes (m^3). Catchment denudation rates (mm y^{-1}) were calculated based on the affected area extend (378,642 m^2).

Interval	Erosion		Deposition		Net change	
	Volume (m^3)	Rates (mm y^1)	Volume (m^3)	Rates (mm y^1)	Volume (m^3)	Volume (m^{3}y^{-1})
2010-2012	3.10 (±0.02) $*10^4$	45	4.237 (±0.006) $*10^4$	5	-2.97 (±0.03) $*10^4$	-1.51 (±0.01) $*10^4$
2012-2014	4.20 (±0.02) $*10^4$	52	1.45 (±0.01) $*10^4$	18	-2.75 (±0.04) $*10^4$	-1.29 (±0.02) $*10^4$
2014-2015	4.20 (±0.02) $*10^4$	52	2.998 (±0.002) $*10^4$	10	-1.24 (±0.03) $*10^4$	-1.59 (±0.04) $*10^4$
2015-2017	2.081 (±0.002) $*10^5$	257	2.36 (±0.01) $*10^5$	291	2.78 (±0.13) $*10^4$	1.30 (±0.06) $*10^4$
2017-2018	9.38 (±0.04) $*10^4$	217	8.20 (±0.04) $*10^4$	189	-1.18 (±0.09) $*10^4$	-1.03 (±0.08) $*10^4$
2018-2020	3.33 (±0.02) $*10^4$	44	3.46 (±0.01) $*10^4$	46	1.21 (±0.43) $*10^3$	6.12 (±2) $*10^2$

4.4. Geomorphic sediment budgets across the sediment cascade

The time series of spatial distribution of differences of DSMs (Figure 7) and differentiated geomorphic sediment budgets (Figure 8) reveals the fast system response to the cliff fall. The concept of sediment continuity refers to the transfer or exchange of sediment across various parts of the hillslope system, which involves the conservation of mass among sediment inputs, stores and output (Joyce et al., 2018). Sediment storages and sinks (marked as (1), (2), (3), and (4) in Figure 7) define the boundaries between different morphodynamic components, which are characterized by slight changes in mean slope that imprints morphological controls on transport processes. Regardless of the existence of depositional landforms, sediment continuity dominates from 2010 until 2014 evidenced in negative net change at all the geomorphic system components.

An initial disruption in the sediment continuity is observed between 2014 and 2015. At the rockface, boulder and block falls occur, which detach from the sub-vertical wall and deposit at its base. Additionally, in the upper channelized erosive debris flow channel, less than $< 10^2\,\mathrm{m}^3$ of recently deposited material (less than two years of residence time) are internally redistributed. However, even during this period of localized disruption, sediment redistribution continues to take place at the widened debris flow channel, which ensures sediment delivery to the outlet into the braided sediment-supercharged Jochbach river.

Following the cliff fall event, there was an immediate disruption of sediment transfer among the different regions of the system, with about 75% of the produced sediment being deposited at the upper channelized erosive debris flow channel. A total of 1.356 ($\pm$0.003) $*10^5\,\mathrm{m}^3$ of sediment were deposited over the 1.5 km length of the upper channelized erosive debris flow channel (Figure 8). Despite the positive sediment budget at the widened disperse debris flow channel, massive deposition occurred at the outlet. The formation of a terrace of almost 3 m evidence the positive net change of 2.60 ($\pm$0.03) $*10^4\,\mathrm{m}^3$. Although the stream power was strong enough to incise the terrace and prevent the formation of a dam, the outlet flood plain was filled with new debris that impacted the dynamics of the riverbed.

A dramatic inversion from deposition to erosion occurs two years after the cliff fall. Sediment waves or slugs deposited 8.14 ($\pm$0.04) $*10^4\,\mathrm{m}^3$ at the apex of the widened dispersive debris flow channel infilling the valley with 3 m of transported material which increased to almost 10 m four years after the cliff fall (supplementary Fig. 2, profile C-C'). Despite the increased sediment input due to the cliff fall, there were reversed net changes between the widened dispersive debris flow channel and outlet four years after the cliff fall (Figure 7). This suggest that the sediment transport processes had not fully recovered to pre-disturbance levels, even though, the sediment continuity within the catchment was restored one year after the initiation of the disturbance, i.e., increased sediment due to the cliff fall.

Earth **Surface**
Dynamics
Discussions
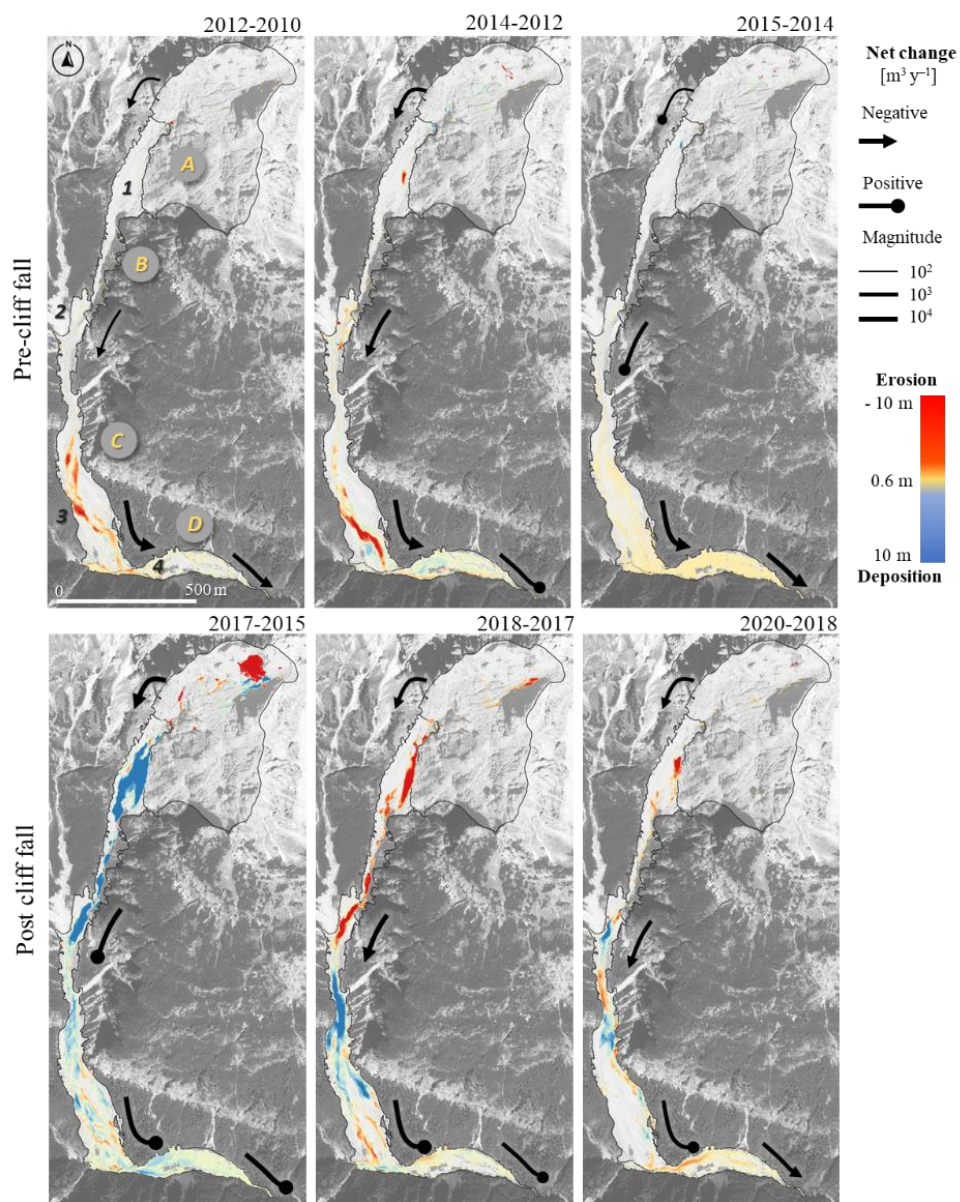
Figure 7. Time-series of spatial distribution of erosional (red) and depositional (blue) areas with black arrows as an indication of sediment continuity based on the net changes. (A) rockface (B) upper channelized debris flow channel, (C) widened dispersed debris flow channel, and (D) outlet to the Jochbach river. (1), (2), (3), and (4) mark the position of morphological blockages that promotes deposition thus attenuation in the sediment flux.

The braided sediment-supercharged Jochbach river incised the 3m terrace formed after the cliff fall by developing

a single fluvial channel confined towards the north side of the alluvial plain, opposite to the pre-event river

channel, located at the south of the alluvial plain. However, a braided channel characterizes the lower outlet sink

Earth **Surface**
Dynamics
Discussions

suggesting an ongoing adjustment to the depleted sediment delivery ratio as a consequence of the cliff fall event.
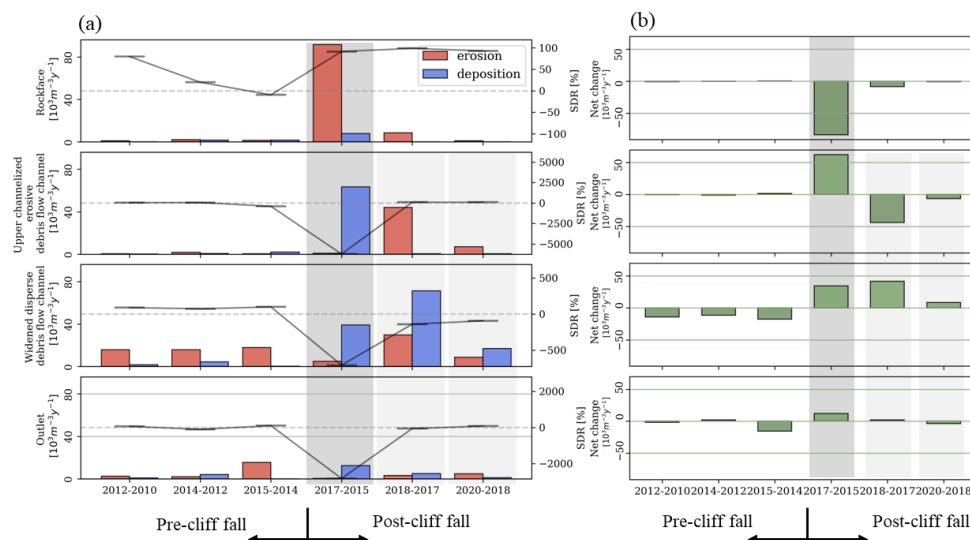
Figure 8. Segregate sediment budget. a) Left axis: Bar plot for net yearly erosion and deposition volumes. Right axis: Sediment delivery ratio. b) net change as an indicator of sediment continuity. Dark grey polygons highlight the temporal stamp at which the cliffs fall took place. Lighter grey indicates the system response two and four years after the event.

5. Discussion

The scarcity of high-magnitude rockfalls limits the understanding of the physical response of mountain catchment to a sudden increased of sediment input. Digital photogrammetry and image-matching algorithms revolutionized the usage of optical sensors to study topographic changes. The recently available high-resolution temporal and spatial datasets provide a fresh look for geomorphic responses and the time lag between disturbance (increased sediment input due to cliff fall) and reaction (geomorphic response: increased sediment transport by means of debris flows) times from which typically short-term responses become a societal concern (Owens et al., 2010). Even though the proposed 3D-coregistration workflow optimizes the DSMs extracted from consecutive nadir view large format aerial surveys for volumetric calculations in steep terrain, there are still limitations on the representation of complex topography. Thus, it requires careful thought about the validity of the measurements. Despite this, the presented results are paramount to identifying and better understanding coupling mechanisms of high-magnitude slope events at a high temporal-spatial resolution to a wide extent. The analysis of within hillslope morphodynamics and its coupling with the fluvial system exemplify the alpine catchment response to future climatic changes and landscape dynamics.

5.1. Validity of measurements

Considering the inhomogeneity of the aerial imagery, the quantitative data described above are comparable to other published results obtained by digital photogrammetry (e.g. (Kaufmann and Ladstädter, 2003; Schiefer and Gilbert, 2007; Marzolff and Poesen, 2009; Fabris and Pesci, 2009; Micheletti et al., 2015; Hilger and Beylich, 2018; Geissler et al., 2021). The authors acknowledge the limitations of aerial imagery to depict vertical surfaces and in particular negative vertical surfaces. Nevertheless, the proposed workflow resulted in consistent landscape

representations through time evidenced by topographic profiles extracted from the DSM and volume calculation of the 2016 cliff fall using all possible DSM combinations (supplementary Table 6). Additionally, the back

425 calculation of the failed volumes from the seismic signals of regional stations (Sec. 4.1.) is in the range of the photogrammetrically determined volumes, thus supporting the results via a second methodological approach.

Even though we followed a very conservative approach, possible overestimations of the volumes are expected, particularly for the rockface where complex topography predominates. When visualizing the point clouds, it is

430 possible to perceive the dense point cloud on the horizontal surfaces, but little to no points on vertical and pseudo-vertical surfaces for some of the datasets (e.g., 2015 dataset). Additionally, even if the vertical sides are completely depicted, the gridded component of the analysis poorly represents the vertical topography. On the other hand, the results on the northern slope (Figure 5a), often acquired under poorer illumination conditions, are prone to higher uncertainty.

435

The 3D-coregistration successfully mitigates spatial discrepancies between surveys and evaluate the relative correspondence of x, y and z in the range of the spatial resolution. A remaining challenge lies in the assessment of the ratio to noise. The segmentation approach was designed to filter topographic changes at each landscape compartment having into account the stated data limitations. Lower uncertainty is achieved at the widened

440 dispersed debris flow channel and outlet due to the smoother surfaces favorable for the photogrammetric reconstruction. In spite of the discussed drawbacks, the presented workflow aims for an efficient and fast calculation of volumetric changes foreseen by the usage of aerial imagery for the early detection of future hazardous areas over wide extents or multiple basins in the context of a fast-changing climate and landscape.

The complementary analysis of seismic datasets elucidates the multi-stage detachment of possibly 6 events with

445 exact timing (3 block falls followed by 3 cliff falls). The latest three seismic events show clear evidence of a source located close to the Hochvogel rock failure, while the first three events are harder to constrain due to their smaller amplitude. Nevertheless, these also show the same intensity-distance decay and signal arrival time patterns and can therefore be considered. Additionally, the respective sub-event´s percentage of the total volume is very similar for the stations OBER, RETA, DAVA, MOTA and A307A (supplementary Fig 6, Table 13). The stations

450 PART and ZUGS must be excluded due to their bad signal-to-noise ratio in the relevant frequency band. For a fall height of 60 m, the volume estimated from the seismic signal at OBER is 20 % lower than that estimated photogrammetrically, but the seismic method neglects detachments that are too small to be recorded by the distant broadband sensor, detachments from the same source area but not belonging to the 3-day event, and energy that gets lost due to fragmentation of the failed mass. The other stations further away underestimate the volume due

455 to stronger signal damping, distortion and worse coupling compared to the closest station OBER.

5.2. Rockfall activity as landscape re-shaping mechanism

Bi-annual rockwall retreat rates for the five years prior to the cliff fall, which averaged 6.5 mm y^{-1}, slightly exceed short-term (< 10 years) rock wall retreats for limestones (Draebing et al., 2022) with a maximum retreat of 9.5 mm y^{-1} between 2012 and 2014. However, they are consistent with previous funding of enhanced rockfall activity

460 for carbonate cliffs (Krautblatter et al., 2012). The (multi-) annual temporal intervals used in this study are unlikely

to be sensible to precursory deformations, however, patterns of erosion across the rockface slope in the years prior to the cliff fall might reveal signs of alert. Close-up observations of the area of the cliff failure evidence block fall and boulder fall at the base of the failure with volumes of 1.71 (±0.005) $*10^3$ m^3 and 1.05 (±0.003) $*10^3$ m^3 in 2012-2014 and 2.91 (±0.01) $*10^2$ m^3 in 2014-2015 reflecting a main deformation area (Kromer et al., 2018). The

465 cliff fall resulted in the rockwall retreat of 390 mm y^{-1} between 2015 and 2017 increasing the mean steepness of the rockface by 1%. The consecutive detachment of at least 6 blockfalls over 3 days follows an increase in magnitude from 10^3 m^3 to 10^4 m^3 previously suggested by other studies (e.g., (Kromer et al., 2017; Rosser et al., 2007; Abellán et al., 2009; Benjamin et al., 2020), and paramount for the understanding of cascading risk in alpine regions.

470

The triggering mechanism for this multi-stage event is hard to constrain and needs further research. Among common triggering factors are precipitation and cyclic thermal stressing (Dietze et al., 2017b). The multi-stage event is preceded by a phase of several dry and hot summer days. In the night before the first block fall, minor amounts of rain have been recorded, but the three final cliff falls on July 11th are preceded by more intense rainfall

475 of up to 1.4 mm/10 min with a time lag of less than 1 h (Figure 4). Also, all recorded events happened during the morning and evening hours where a strong thermal gradient might have an influence on the stressing of the rock mass (Dietze et al., 2017b, 2021).

5.3. Mechanism of sediment delivery continuity.

The fast system reaction time of 1 to 2 years is evidenced by the massive inversion from a depositional regimen

480 (2015-2017) to an erosive regime (2017-2018) which mobilizes sediment through the system with short temporal residence times in the sediment cascading. The material detached by the cliff fall entrained older deposits at the upper channelized erosive debris channel, which we traced back to 1945 by the visual inspection of historical aerial imagery, increasing the amount of transported sediment downslope. Despite the remobilization of older deposits, more than 10 m of recently deposited sediment remains at the upper channelized debris channel which

485 serves as a source for future debris flows and possibly extends the system relaxation times according to recent numerical simulations (Heckmann and Schwanghart, 2013) as the main mechanism of sediment transport in the studied catchment is debris flows.

Observations in the Swiss Alps suggest increased debris flow activity after a sudden sediment input from a rock

490 avalanche or large landslides (Baer et al., 2017; Frank et al., 2019). Debris flows are a common process in the studied catchment before the cliff fall event, but spatially confined to the widened dispersed debris flow channel where sediment availability is high. On the contrary, increased sediment remobilization is clearly triggered at the upper channelized erosive debris flow channel shortly after the cliff fall, acting as an efficient process to restore sediment continuity. A systematic study of six catchments in Switzerland affected by landslides that generated

495 new sediment deposits suggests a considerable increase in debris-flow frequency for one to eight years following the landslide with no clear rain-fall-related apparent trigger (Frank et al., 2019). For the studied catchment, relaxation times exceed the observation time thus we plan to continue with the monitoring.

Debris flows are normally triggered by short-duration and high-intensity rainstorms. A study in the Zermatt Valley
500   (Swiss Alps) concluded that the occurrence of debris flows would depend on short-term changes in triggering
rainfall rather than on long-term climatic changes (Bollschweiler and Stoffel, 2010), thus high-resolution temporal
and spatial analysis are paramount to better assess the cascading natural hazard of rock slope failures. A review
of nine debris flow monitored sites around the world suggests that hourly rainfall intensities between 5 and 15
mm/h are sufficient to trigger debris flows (Hürlimann et al., 2019). Particularly, at Illgraben basin, Switzerland,
505   sediment transport was reported at rainfall intensity of 2.2 mm/10 min while debris flows were initiated in a range
between 3.8 to 9.6 mm/10 min. Precipitation stations at the vicinity of the Hochvogel (Hinterhornbach/AUS -
Station ID:6290) display increased mean seasonal (April-November) rainfall intensity over the last decade for
events with a duration less than 4 hours (Figure 9). The frequency of rainstorms exceeding 10mm/h, 3.8
mm/10min, and 9.6mm/10min are higher for the time interval when the cliff fall occurred (2015-2017: T4). The
510   marked depositional regimen obscures the possible within slope impact of rainstorm increased frequency on debris
flow activity, nonetheless, it might be reflected in the Jochbach stream power to erode the almost 3-meter terrace
that incipiently blocked the outlet, preventing the blockade of the river system. Even though the massive erosive
regimen subsequent to the cliff fall is characterized by rainfall frequencies similar to those pre-cliff falls (6 to 7
days with more than 10mm/h), the increased mean rainstorm intensity might play a role in the fast response times
515   of the system.
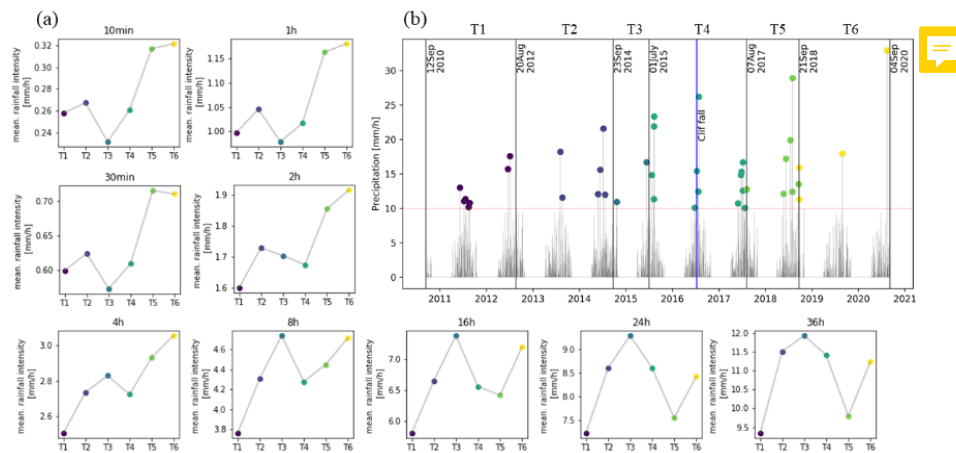
Figure 9. Intensity-duration and frequency analysis for a diversity of rainfall events measured at the precipitation
station 6290-Hinterhornbach/AUS. Data basis: Deutscher Wetterdienst, cumulative sum over individual values. The
analysis was performed by segmenting the rainfall datasets by the acquisition dates of the aerial imagery being:
520   T1, T2, and T3, the years before the cliff fall plotted in dark colors; T4 the mean rainfall after, during and one year
after the cliff fall in light green; and T5 and T6 the time intervals with increased erosion in light green and yellow.

Debris flow inferred trajectories evidence short travel distances (<500 m) promoting the sediment transfer within
the slope morphodynamic components but rarely reaching the outlet. Empirical relationships express the runout
distance of debris flows in terms of topography and volume of mass (Rickenmann, 2005; Hürlimann et al., 2008).
525   Sediment storages and sinks (marked as (1), (2), (3), and (4) in Figure 7) spatially correspond to slope changes
that decrease flow energy thus debris flow travel distances. Regardless of the temporal lumping, multiple debris
flow events were visually identified on the orthophotos based on differences in color and granulometry, but a
complete separation remains challenging.

530 The formation of at least three levels of terraces with predominance course sediment after the cliff fall evidence
the fluvial response to the decreased sediment flux at the outlet. The channelization of the river channel increases
the stream erosion power thus possible lateral erosion downstream. Hence, the effects of the cliff fall event are
seen not only in the higher erosive regimen at the hillslope but also in the morphodynamic adjustment of the
Jochbach river. A remaining key question deals with the conditions, mechanism, and timing required to reestablish

535 the pre-event morphodynamics. Currently, sediment storages resulting from geomorphic processes such as high
magnitude slope instability and paraglacial and glacier sediment storages, are often landforms decoupled from the
present-day geomorphic process. In the context of increased rainfall activity, the couple/reconnection of those
systems and their magnitude and persistence will become key parameters for the management and development
of alpine communities.

540

6. Conclusions

The combination of seismic information and temporal series of high-resolution wide-extent true-orthophotos and
DSMs provide an accurate assessment of the temporal and special evolution of rockfalls and the subsequent

545 massive sediment redistribution. A multi-stage detachment of more than 150,000 m^3 in the Hochvogel summit,
northern calcareous alps (DE/AT), was responsible for the production of 97% of the total sediment eroded between
2010 and 2020. We identified a significant disproportion in the contribution of rockfall magnitudes for the four
slopes that constitute the summit with predominance of debris falls for the northern and western slopes, while the
southeaster slope has a large proportion of boulder fall, thus, increased hazard. The seismic analysis revealed

550 consecutive blockfalls with increased magnitude from 10^3 to 10^4 m^3 in a time period of 3 days during the summer
of 2016, strongly increasing the rockfall risk in the area. Therefore, these results enhance the need of monitoring
alpine slopes to better assess possible increased rockfall activity that leads to safety concerns. We suggest the
integration of wide-extend photogrammetric datasets in future alpine early warning system.

555 The time series of spatial distribution of differences of DSM and differentiated geomorphic sediment budgets
contributes to a better understanding of the complex nature and feedback of cascading processes. The alpine
catchment quickly responded to the cliff fall within 0 to 4 years, resulting in massive sediment redistribution
within the catchment and reduction in sediment delivery to the outlet. This, in turn, modified the fluvial response
at the catchment outlet. Sediment continuity/transfer within the hillslope was rapidly recovered two years

560 following the cliff fall. The recovered sediment flux mobilizes sediment along the geomorphic subsystems;
however, the sediment waves were inefficient in delivering sediment to the catchment outlet. Relaxation times are
expected beyond 10 years given that the latest observations (2020) still revealed perturbation in the system and
the deposition of up to 10 m of sediment at the upper channelized debris flow which serves as a sediment input
for future debris flows.

565

The results present the first step towards a better understanding, prediction, and early warning of alpine natural
hazards under expected extreme climatic conditions. The ongoing interdisciplinary AlpSenseRely project aims to
integrate high-resolution multi-scale, multi-temporal remote sensing data (Large format digital aerial

570 photogrammetry and UAV) for an accurate quantification of temporal and spatial changes in alpine geomorphic systems.

Data Availability

The original aerial imagery is available at Landesamt für Digitalisierung, Breitband und Vermessung (LDBV), Bundesamt für Eich- und Vermessungswesen (BEV), and 3D RealityMaps GmbH upon request. Precipitation data is freely available at the Geoportal from the Deutscher Wetterdienst (https://dwd-geoportal.de/). Seismic data is
575 freely available at reported sources in the supplementary material.

Author contributions

N.B. wrote the manuscript with contributions from J.L.
N.B. developed the topographic time series workflow, analyzed the data and compiled results
J.L. calculated seismic volumes
580 J.J. created DSM and orthophotos from digital aerial imagery
M.D. verified and advised on the implementation of the seismic volume's calculation
U.M, F.S and M.K provided guidance and funding
All authors checked and revised the text and the figures of the manuscript and contributed to the ideas developed in this study.

585 **Competing interests**

An author is a member of the editorial board of the journal Earth Surface Dynamics. The peer-review process was guided by an independent editor, and the authors have also no other competing interest to declare.

Acknowledgments

We thank the Land Tyrol and particularly Mag. Thomas Figl for the open sharing of the pictures taken during the
590 aerial inspection of the Hochvogel before the cliff fall which helped us to better picture the magnitude of the detachment, the Landslide research group at TUM for the fieldwork support during the UAV acquisitions, particularly to Andreas Dietrich for the UAV acquisition on 2017. We are indebted to Peter Mederer for his contribution to the early developments of the 3D-coregistration python workflow during his internship at 3D RealityMaps GmbH, and the colleagues at 3D RealityMaps GmbH, Munich for the outstanding support with the
595 implementation of the 3D models used for visualization, visual interpretation, and figures.

Financial support

This research was funded by the Bavarian Ministry of Environment and Consumer Protection in the framework of the project "AlpSenseRely" Alpine remote sensing of climate-induced natural hazards: Reliability of multi-method hazard prediction in a changing climate (Teilprojekt TUSO1UFS-77318). Initial datasets were acquired
600 during the project 'AlpSenseBench' Alpine remote sensing of climate-induced natural hazards funded by the Bavarian Ministery of Economic Affairs, Regional Development and Energy (grant no. 45-6723a/15/2).

References

Abellán, A., Jaboyedoff, M., Oppikofer, T., and Vilaplana, J. M.: Detection of millimetric deformation using a
605 terrestrial laser scanner: experiment and application to a rockfall event, Nat Hazard Earth Sys, 9, 365–372, https://doi.org/10.5194/nhess-9-365-2009, 2009.

Anderson, S. W.: Uncertainty in quantitative analyses of topographic change: error propagation and the role of thresholding, Earth Surf Processes, 44, 1015–1033, https://doi.org/10.1002/esp.4551, 2019.

610 Baer, P., Huggel, C., McArdell, B. W., and Frank, F.: Changing debris flow activity after sudden sediment input: a case study from the Swiss Alps, Geology Today, 33, 216–223, https://doi.org/10.1111/gto.12211, 2017.

Benda, L. E. and Dunne, T.: Stochastic Forcing of Sediment Routing and Storage in Channel Networks, Water Resources Research, 33, 2865–2880, https://doi.org/10.1029/97wr02387, 1997.

Benjamin, J., Rosser, N. J., and Brain, M. J.: Emergent characteristics of rockfall inventories captured at a regional scale, Earth Surf Processes, 45, 2773–2787, https://doi.org/10.1002/esp.4929, 2020.

615 Bollschweiler, M. and Stoffel, M.: Changes and trends in debris-flow frequency since AD 1850: Results from the Swiss Alps, Holocene, 20, 907–916, https://doi.org/10.1177/0959683610365942, 2010.

Burt, T. P. and Allison, R. J.: Sediment Cascades. An Integrated Approach, First edition., John Wiley & Sons, Ltd, 2010.

Clapuyt, F., Vanacker, V., Christl, M., Oost, K. V., and Schlunegger, F.: Spatio-temporal dynamics of sediment
620 transfer systems in landslide-prone Alpine catchments, Solid Earth, 10, 1489–1503, https://doi.org/10.5194/se-10-1489-2019, 2019.

CloudCompare v2.0: A software for processing and comparing 3D point clouds: http://www.cloudcompare.com.

DAV, D.: Neue Felsstürze vom Hochvogel ins Weittal, Juli 2016 | Neue Felsstürze vom Hochvogel ins Weittal, 2016.

625 DAV, D.: Chronik - Sperrung des Bäumenheimer Weges, Sperrung Bäumenheimer Weg, 2017.

Dietze, M., Mohadjer, S., Turowski, J. M., Ehlers, T. A., and Hovius, N.: Seismic monitoring of small alpine rockfalls – validity, precision and limitations, Earth Surf Dynam, 5, 653–668, https://doi.org/10.5194/esurf-5-653-2017, 2017a.

Dietze, M., Turowski, J. M., Cook, K. L., and Hovius, N.: Spatiotemporal patterns, triggers and anatomies of
630 seismically detected rockfalls, Earth Surf Dynam, 5, 757–779, https://doi.org/10.5194/esurf-5-757-2017, 2017b.

Dietze, M., Krautblatter, M., Illien, L., and Hovius, N.: Seismic constraints on rock damaging related to a failing mountain peak: the Hochvogel, Allgäu, Earth Surf. Process. Landforms, 46, 417–429, https://doi.org/10.1002/esp.5034, 2021.

Draebing, D., Mayer, T., Jacobs, B., and McColl, S. T.: Alpine rockwall erosion patterns follow elevation-
635 dependent climate trajectories, Commun Earth Environ, 3, 21, https://doi.org/10.1038/s43247-022-00348-2, 2022.

Dussauge-Peisser, C., Helmstetter, A., Grasso, J.-R., Hantz, D., Desvarreux, P., Jeannin, M., and Giraud, A.: Probabilistic approach to rock fall hazard assessment: potential of historical data analysis, Nat Hazard Earth Sys, 2, 15–26, https://doi.org/10.5194/nhess-2-15-2002, 2002.

640 Eltner, A. and Sofia, G.: Structure from motion photogrammetric technique, in: Developments in Earth surface process, vol. 23, edited by: Tarolli, P. and Mudd, S. M., 1–24, https://doi.org/https://doi.org/10.1016/B978-0-444-64177-9.00001-1, 2020.

Erismann, T. H. and Abele, G.: Dynamics of Rockslides and Rockfalls, Springer Science & Business Media, Heidelberg, 2001.

645 Fabris, M. and Pesci, A.: Automated DEM extraction in digital aerial photogrammetry: precisions and validation for mass movement monitoring, Ann Geophys-italy, 48, https://doi.org/10.4401/ag-3247, 2009.

Fischer, L., Purves, R. S., Huggel, C., Noetzli, J., and Haeberli, W.: On the influence of topographic, geological and cryospheric factors on rock avalanches and rockfalls in high-mountain areas, Nat Hazard Earth Sys, 12, 241–254, https://doi.org/10.5194/nhess-12-241-2012, 2012.

650 Frank, F., Huggel, C., McArdell, B. W., and Vieli, A.: Landslides and increased debris-flow activity: A systematic comparison of six catchments in Switzerland, Earth Surf Processes, 44, 699–712, https://doi.org/10.1002/esp.4524, 2019.

Fryirs, K.: (Dis)Connectivity in catchment sediment cascades: a fresh look at the sediment delivery problem, Earth Surf Processes, 38, 30–46, https://doi.org/10.1002/esp.3242, 2013.

655 Fuchs, F., Lenhardt, W., Bokelmann, G., and Group, the A. W.: Seismic detection of rockslides at regional scale: examples from the Eastern Alps and feasibility of kurtosis-based event location, Earth Surf Dynam, 6, 955–970, https://doi.org/10.5194/esurf-6-955-2018, 2018.

Geissler, J., Mayer, C., Jubanski, J., Münzer, U., and Siegert, F.: Analyzing glacier retreat and mass balances using aerial and UAV photogrammetry in the Ötztal Alps, Austria, Cryosphere, 15, 3699–3717,
660 https://doi.org/10.5194/tc-15-3699-2021, 2021.

Gregory, K. J. and Lewin, J.: The Basics of Geomorphology: Key Concepts, https://doi.org/10.4135/9781473909984, 2014.

Guerin, A., Ravanel, L., Matasci, B., Jaboyedoff, M., and Deline, P.: The three-stage rock failure dynamics of the Drus (Mont Blanc massif, France) since the June 2005 large event, Sci Rep-uk, 10, 17330,
665 https://doi.org/10.1038/s41598-020-74162-1, 2020.

Haala, N. and Rothermel, M.: Dense Multi-Stereo Matching for High Quality Digital Elevation Models, Photogrammetrie - Fernerkundung - Geoinformation, 2012, 331–343, https://doi.org/10.1127/1432-8364/2012/0121, 2012.

Hantz, D., Corominas, J., Crosta, G. B., and Jaboyedoff, M.: Definitions and Concepts for Quantitative Rockfall
670 Hazard and Risk Analysis, Geosciences, 11, 158, https://doi.org/10.3390/geosciences11040158, 2021.

Heckmann, T. and Schwanghart, W.: Geomorphic coupling and sediment connectivity in an alpine catchment — Exploring sediment cascades using graph theory, Geomorphology, 182, 89–103, https://doi.org/10.1016/j.geomorph.2012.10.033, 2013.

Heckmann, T., Bimböse, M., Krautblatter, M., Haas, F., Becht, M., and Morche, D.: From geotechnical analysis
675 to quantification and modelling using LiDAR data: a study on rockfall in the Reintal catchment, Bavarian Alps, Germany, Earth Surf Processes, 37, 119–133, https://doi.org/10.1002/esp.2250, 2012.

Heckmann, T., Hilger, L., Vehling, L., and Becht, M.: Integrating field measurements, a geomorphological map and stochastic modelling to estimate the spatially distributed rockfall sediment budget of the Upper Kaunertal, Austrian Central Alps, Geomorphology, 260, 16–31, https://doi.org/10.1016/j.geomorph.2015.07.003, 2016.

680 Heißel, G. and Figl, T.: Stellungnahme der Amtssachverständigen für Geologie, Hydrogeologie und technische Geologie, sowie für den Schutz vor Erosion und vor alpinen geogenen Naturgefahren, 2017.

Hibert, C., Mangeney, A., Grandjean, G., and Shapiro, N. M.: Slope instabilities in Dolomieu crater, Réunion Island: From seismic signals to rockfall characteristics, J Geophys Res Earth Surf, 116, https://doi.org/10.1029/2011jf002038, 2011.

685   Hilger, L. and Beylich, A. A.: Geomorphology of Proglacial Systems, Landform and Sediment Dynamics in Recently Deglaciated Alpine Landscapes, Geogr Phys Environ, 251–269, https://doi.org/10.1007/978-3-319-94184-4_15, 2018.

Hirschmuller, H.: Stereo Processing by Semiglobal Matching and Mutual Information, Ieee T Pattern Anal, 30, 328–341, https://doi.org/10.1109/tpami.2007.1166, 2008.

690   Hungr, O., McDougall, S., Wise, M., and Cullen, M.: Magnitude–frequency relationships of debris flows and debris avalanches in relation to slope relief, Geomorphology, 96, 355–365, https://doi.org/10.1016/j.geomorph.2007.03.020, 2008.

Hürlimann, M., Rickenmann, D., Medina, V., and Bateman, A.: Evaluation of approaches to calculate debris-flow parameters for hazard assessment, Eng Geol, 102, 152–163, https://doi.org/10.1016/j.enggeo.2008.03.012, 695   2008.

Hürlimann, M., Coviello, V., Bel, C., Guo, X., Berti, M., Graf, C., Hübl, J., Miyata, S., Smith, J. B., and Yin, H.-Y.: Debris-flow monitoring and warning: review and examples, Earth-sci Rev, 199, 102981, https://doi.org/10.1016/j.earscirev.2019.102981, 2019.

Jakob, M.: A size classification for debris flows, Eng Geol, 79, 151–161, 700   https://doi.org/10.1016/j.enggeo.2005.01.006, 2005.

James, L. A., Hodgson, M. E., Ghoshal, S., and Latiolais, M. M.: Geomorphic change detection using historic maps and DEM differencing: The temporal dimension of geospatial analysis, Geomorphology, 137, 181–198, https://doi.org/10.1016/j.geomorph.2010.10.039, 2012.

Joyce, H. M., Hardy, R. J., Warburton, J., and Large, A. R. G.: Sediment continuity through the upland sediment 705   cascade: geomorphic response of an upland river to an extreme flood event, Geomorphology, 317, 45–61, https://doi.org/10.1016/j.geomorph.2018.05.002, 2018.

Kaufmann, V. and Ladstädter, R.: Quantitative analysis of rock glacier creep by means of digital photogrammetry using multi-temporal aerial photographs: Two case studies in the Austrian Alps, in: Proceedings of the 8th International Conference on Permafrost, 525–530, 2003.

710   Kazhdan, M., Chuang, M., Rusinkiewicz, S., and Hoppe, H.: Poisson Surface Reconstruction with Envelope Constraints, Comput Graph Forum, 39, 173–182, https://doi.org/10.1111/cgf.14077, 2020.

Korup, O., Densmore, A. L., and Schlunegger, F.: The role of landslides in mountain range evolution, Geomorphology, 120, 77–90, https://doi.org/10.1016/j.geomorph.2009.09.017, 2010.

Krautblatter, M., Moser, M., Schrott, L., Wolf, J., and Morche, D.: Significance of rockfall magnitude and 715   carbonate dissolution for rock slope erosion and geomorphic work on Alpine limestone cliffs (Reintal, German Alps), Geomorphology, 167, 21–34, https://doi.org/10.1016/j.geomorph.2012.04.007, 2012.

Kromer, R., Lato, M., Hutchinson, D. J., Gauthier, D., and Edwards, T.: Managing rockfall risk through baseline monitoring of precursors using a terrestrial laser scanner, Can Geotech J, 54, 953–967, https://doi.org/10.1139/cgj-2016-0178, 2017.

720   Kromer, R. A., Rowe, E., Hutchinson, J., Lato, M., and Abellán, A.: Rockfall risk management using a pre-failure deformation database, Landslides, 15, 847–858, https://doi.org/10.1007/s10346-017-0921-9, 2018.

Lacroix, P. and Helmstetter, A.: Location of Seismic Signals Associated with Microearthquakes and Rockfalls on the Séchilienne Landslide, French AlpsLocation of Seismic Signals Associated with Microearthquakes and Rockfalls on Séchilienne Landslide, B Seismol Soc Am, 101, 341–353, https://doi.org/10.1785/0120100110, 725   2011.

Leinauer, J., Jacobs, B., and Krautblatter, M.: Anticipating an imminent large rock slope failure at the Hochvogel (Allgäu Alps), Geomechanics Tunn, 13, 597–603, https://doi.org/10.1002/geot.202000027, 2020.

Leinauer, J., Jacobs, B., and Krautblatter, M.: High alpine geotechnical real time monitoring and early warning at a large imminent rock slope failure (Hochvogel, GER/AUT), Iop Conf Ser Earth Environ Sci, 833, 012146,
730   https://doi.org/10.1088/1755-1315/833/1/012146, 2021.

Le Roy, G. L., Helmstetter, A., Amitrano, D., Guyoton, F., and Roux-Mallouf, R. L.: Seismic Analysis of the Detachment and Impact Phases of a Rockfall and Application for Estimating Rockfall Volume and Free-Fall Height, J Geophys Res Earth Surf, 124, 2602–2622, https://doi.org/10.1029/2019jf004999, 2019.

Manconi, A., Picozzi, M., Coviello, V., Santis, F. D., and Elia, L.: Real-time detection, location, and
735   characterization of rockslides using broadband regional seismic networks, Geophys Res Lett, 43, 6960–6967, https://doi.org/10.1002/2016gl069572, 2016.

Marzolff, I. and Poesen, J.: The potential of 3D gully monitoring with GIS using high-resolution aerial photography and a digital photogrammetry system, Geomorphology, 111, 48–60, https://doi.org/10.1016/j.geomorph.2008.05.047, 2009.

740   McSaveney, M. J.: Recent rockfalls and rock avalanches in Mount Cook National Park, New Zealand, in: Catastrophic Landslides Effects, ocurrences and Mechanisms, vol. XV, Geological Society of America, https://doi.org/https://doi.org/10.1130/REG15, 2002.

Mergili, M., Jaboyedoff, M., Pullarello, J., and Pudasaini, S. P.: Back calculation of the 2017 Piz Cengalo–Bondo landslide cascade with r.avaflow: what we can do and what we can learn, Nat Hazard Earth Sys, 20, 505–
745   520, https://doi.org/10.5194/nhess-20-505-2020, 2020.

Micheletti, N., Lane, S. N., and Chandler, J. H.: Application of archival aerial photogrammetry to quantify climate forcing of alpine landscapes, Photogrammetric Rec, 30, 143–165, https://doi.org/10.1111/phor.12099, 2015.

NNZ: Die Murgänge bei Bondo kosten rund 41 Millionen Franken, , 14th December, 2017.

750   Owens, P. N., Petticrew, E. L., and Perk, M. van der: Sediment response to catchment disturbances, J Soils Sediments, 10, 591–596, https://doi.org/10.1007/s11368-010-0235-1, 2010.

Rickenmann, D.: Debris-flow Hazards and Related Phenomena, Springer Praxis Books, 305–324, https://doi.org/10.1007/3-540-27129-5_13, 2005.

Riggs, H. C.: Frequency Curves, US Government Printing Office, 1968.

755   Rosser, N., Lim, M., Petley, D., Dunning, S., and Allison, R.: Patterns of precursory rockfall prior to slope failure, J Geophys Res Earth Surf 2003 2012, 112, https://doi.org/10.1029/2006jf000642, 2007.

Rothermel, M., Wenzel, K., Fritsch, D., and Haala, N.: SURE: Photogrammetric surface reconstruction from imagery, in: Proceedings LC3D Workshop, 615–620, 2012.

Schiefer, E. and Gilbert, R.: Reconstructing morphometric change in a proglacial landscape using historical
760   aerial photography and automated DEM generation, Geomorphology, 88, 167–178, https://doi.org/10.1016/j.geomorph.2006.11.003, 2007.

Schrott, L., Hufschmidt, G., Hankammer, M., Hoffmann, T., and Dikau, R.: Spatial distribution of sediment storage types and quantification of valley fill deposits in an alpine basin, Reintal, Bavarian Alps, Germany, Geomorphology, 55, 45–63, https://doi.org/10.1016/s0169-555x(03)00131-4, 2003.

765 Thiele, S. T., Grose, L., Samsu, A., Micklethwaite, S., Vollgger, S. A., and Cruden, A. R.: Rapid, semi-automatic fracture and contact mapping for point clouds, images and geophysical data, Solid Earth, 8, 1241–1253, https://doi.org/10.5194/se-8-1241-2017, 2017.

Tucker, G. E.: Drainage basin sensitivity to tectonic and climatic forcing: implications of a stochastic model for the role of entrainment and erosion thresholds, Earth Surf Processes, 29, 185–205,
770 https://doi.org/10.1002/esp.1020, 2004.

Walling, D. E. and Collins, A. L.: The catchment sediment budget as a management tool, Environ Sci Policy, 11, 136–143, https://doi.org/10.1016/j.envsci.2007.10.004, 2008.

Whalley, B.: The mechanics of high-magnitude low-frequency rock failure and its importance in a mountainous area, Reading Geographical Papers, 1974.

775 Whalley, B.: Rockfalls, Slope Instability, Chapter 7, 1984.

Wheaton, J. M., Brasington, J., Darby, S. E., and Sear, D. A.: Accounting for uncertainty in DEMs from repeat topographic surveys: improved sediment budgets, Earth Surf Processes, 35, 136–156, https://doi.org/10.1002/esp.1886, 2010.

Wichmann, V., Heckmann, T., Haas, F., and Becht, M.: A new modelling approach to delineate the spatial
780 extent of alpine sediment cascades, Geomorphology, 111, 70–78, https://doi.org/10.1016/j.geomorph.2008.04.028, 2009.